Photocatalytic Degradation of RhB by Fluorinated Bi$_2$WO$_6$ and Distributions of the Intermediate Products

HONGBO FU,[†] SHICHENG ZHANG,[†] TONGGUANG XU,[‡] YONGFA ZHU,*,[‡] AND JIANMIN CHEN*,[†]

Department of Environmental Science and Engineering, Fudan University, Shanghai 200433, People's Republic of China, and Department of Chemistry, Tsinghua University, Beijing 100084, People's Republic of China;

Fluorinated Bi$_2$WO$_6$ catalyst was synthesized by a simple hydrothermal process. The effects of fluorine doping on crystal structure, optical property, photoinduced hydrophilicity, surface acidity, and photocatalytic activity of the as-prepared sample were observed in detail. Fluorinated Bi$_2$WO$_6$ presented the enhanced photoactivity for the RhB degradation under the simulative sunlight ($\lambda > 290$ nm), which could be a synergetic effect of the surface fluorination and the doping of crystal lattice. To get a better handle on the mechanistic details of this photocatalytic system, the photodegradation process of RhB was examined. In the fluorinated Bi$_2$WO$_6$ system, five intermediates, namely, *N,N*-diethyl-*N'*-ethylrhodamine, *N,N*-diethylrohodamine, *N*-ethyl-*N'*-ethylrhodamine, *N*-ethylrhodamine, and rhodamine were thus identified, whereas the first three intermediates could only be identified in the case of the Bi$_2$WO$_6$ system. This result indicated that more RhB molecules were degraded via the deethylation process in the fluorinated Bi$_2$WO$_6$ system. It was proposed that the F$^-$-containing function on the catalyst surface could serve as an electron-trapping site and enhance interfacial electron-transfer rates by tightly holding trapped electrons. On the basis of the experimental results, a photocatalytic mechanism was discussed in detail.

1. Introduction

Semiconductor photocatalytic processes have been widely applied as techniques of destruction of organic pollutants in wastewater and effluents. To date, the major research on photocatalytic oxidation techniques is focus on TiO$_2$, as it is of low cost, is environmentally friendly, and has high stability (*1*). Very recently, some tungstates such as Bi$_2$WO$_6$ and ZnWO$_4$ have also presented high photoactivities for the pollutant degradation (*2–8*). Their unique combination of physical and chemical properties, in terms of molecular and electronic versatility, reactivity, and stability, make us have reason to believe they may be a promising class of photocatalysts for use in degrading organic pollutants.

A major limitation of achieving high photocatalytic efficiency in semiconductor systems is the quick recombination of charge carriers. Recombination, which has faster kinetics than surface redox reactions, is a major drawback as it reduces the quantum efficiency of photocatalysis. Therefore, ways to minimize the recombination rate are important if we are interested in maximizing the photocatalysis efficiency. For this purpose, fluorinated TiO$_2$ has been investigated in relation to doping (TiO$_{2-x}$F$_x$) or surface complexation (F–TiO$_2$) (*9–13*). Hattori et al. reported that fluoride doping improves the crystallinity of anatase and the photocatalytic reactivity. In addition, TiO$_{2-x}$F$_x$ has fewer anion vacancies with a lower density of midgap states and is more stable against photocorrosion (*9*). Yu et al. proposed that the doping F$^-$ ions convert Ti^{4+} to Ti^{3+} by charge compensation and that the presence of a certain amount of Ti^{3+} reduces the electron–hole recombination rate and thus enhances the photocatalytic activity (*10*). Recent study confirmed that F-doping in TiO$_2$ can also induce a visible photocatalytic activity by the creation of oxygen vacancies (*11*). On the other hand, surface fluorination of TiO$_2$ is a simple ligand exchange between F$^-$ ions and surface hydroxyl groups on TiO$_2$. It was reported that the surface fluorination of TiO$_2$ improves the photocatalytic oxidation rate of phenol and tetramethylammonium at a specific pH range (*12*). Since the surface fluorides themselves should not be reactive with valence band (VB) holes [$E°(\text{F}^\bullet/\text{F}^-) = 3.6$ V vs NHE], the higher photocatalytic oxidation rate in the F–TiO$_2$ suspension has been ascribed to the enhanced generation of mobile free OH radicals. Park and Choi reported that surface fluorination of TiO$_2$ changes not only the photodegradation rate of the pollutant but also the mechanistic pathways of the pollutant degradation, as well as the intermediates and product distribution subsequently (*13*).

More recently, a few F-doped non-TiO$_2$ catalysts also exhibited a similar enhancement of photocatalytic activities. F-doped SrTiO$_3$ shows about three times the photocatalytic activity compared with that of undoped SrTiO$_3$ (*14*). The enhancement of photocatalytic activity was mainly ascribable to the formation of oxygen vacancies and increase of effective electron mobility. Fluorine interstitially doped ZnWO$_4$ has been reported recently by our group (*8*). The doping fluorine ions could increase the coordination sphere around the W atom in a WO$_6$ octahedron and cause the distortion of the WO$_6$ octahedron in a ZnWO$_4$ crystal, resulting in an increased transfer rate of photogenerated electrons to the photocatalyst surface and the enhanced photoactivity for rhodamine B (RhB) degradation. On the basis of these results, it could be inferred that the introduction of fluorine, irrespective of the approaches of fluorination, really enhanced the activity of photocatalysts.

We report herein the photocatalytic performances of fluorinated Bi$_2$WO$_6$ prepared by a hydrothermal process. Bulk and surface characterizations of the resulting powders were carried out by means of X-ray diffraction (XRD), determination of Brunauer–Emmett–Teller (BET) specific surface areas, porosity measurements, and diffuse reflectance spectroscopy (DRS) techniques. A RhB dye was used as a model to examine the activity of the photocatalyst. To provide an overall understanding of the reaction pathway(s), high-performance liquid chromatography (HPLC), liquid chromatography/mass spectrometry (LC-MS), and gas chromatography/mass spectrometry (GC-MS) were exploited to identify the *N*-dealkylated intermediates and the final products of RhB from ring cleavage during the photodegradation. This work may provide new insights and under-

* Address correspondence to either author. E-mail: zhuyf@mail.tsinghua.edu.cn (Y.Z.); jmchen@fudan.edu.cn (J.C.).
[†] Fudan University.
[‡] Tsinghua University.

standing on the photocatalytic mechanisms of the fluorination of non-TiO$_2$ catalysts.

2. Experimental Section

2.1. Materials and Sample Preparation. Fluorinated Bi$_2$WO$_6$ samples were prepared by a two-step hydrothermal process. The starting materials of WO$_3$, Na$_2$O, and NaF were mixed and calcined at 1100 °C. The final Na$_2$WO$_4$ containing F$^-$ ions was obtained from XRD patterns (see Supporting Information, Figure S1). In what followed, the value of R_F was used to describe the molar ratio of NaF to Na$_2$O; these were 0, 0.1, 0.2, 0.4, and 0.6 nominal ratios. The calcined sample and Bi(NO$_3$)$_3$ (the molar ratio of 1:1) were used to synthesize fluorinated Bi$_2$WO$_6$ by a hydrothermal process as described in our previous report (*3*). The resulting products were collected by filtration and then were washed by deionized water several times until no F$^-$ ions were left in the solution as tested. The samples were then dried at 80 °C for 4 h for characterization. TEM and HRTEM images of the typical sample (R_F = 0.4) show that the crystals are sheet-shaped (see Supporting Information, Figure S2 and Figure S3). All chemicals used were analytical grade reagents without further purification. Deionized water was used throughout this study.

2.2. Characterization. X-ray diffraction patterns of the powders were recorded at room temperature by a Bruker D8 Advance X-ray diffractometer using Cu Kα radiation and a 2θ scan rate of 2 min^{-1}. The diffuse reflectance absorption spectra of the samples were recorded on a UV−visible spectrophotometer (Hitachi UV-3100) equipped with an integrated sphere attachment. BET surface area measurements were performed by a Micromeritics (ASAP 2010 V5.02H) surface area analyzer. The nitrogen adsorption and desorption isotherms were measured at −196 °C after degassing the samples on a Sorptomatic 1900 Carlo Erba instrument. A photoinduced change of water contact angle (CA) was measured by a commercial contact angle meter (DropMaster 300, Kyowa Interface Science, Japan) at ambient condition, and UV irradiation was produced by a black lamp bulb. To observe the surface acidity of the as-prepared sample, temperature-programmed desorption (TPD) of the preadsorbed pyridine was performed in a vacuum chamber equipped with a Nicolet 470 FTIR spectrometer with a MCT/B infrared detector.

2.3. Photocatalytic Experiments. The photocatalytic activities of the as-prepared samples for the degradation of RhB in solution were tested under the simulative sunlight. A 500 W xenon lamp (λ > 290 nm, CHF-XM-500 W, the Trusttech. Co. Ltd., Beijing) was used as light source, and the average light intensity was 50 mW·cm^{-2}.In a 100 mL suspension containing 2 × 10^{-5} M RhB, 100 mg of the powder samples was dispersed in a rectangular vessel. Prior to irradiation, the suspensions were magnetically stirred in the dark for 0.5 h to ensure the establishment of an adsorption−desorption equilibrium. The suspensions were kept under constant air-equilibrated conditions before and during the irradiation. At given time intervals, 1 mL aliquots were sampled and centrifuged to remove the particles. The filtrates were analyzed by recording the variations in the absorption band (553 nm) in the UV−visible spectra of RhB using a Hitachi U-3010 UV−vis spectrometer.

2.4. Analyses of Intermediate Products. The *N*-dealkylated intermediates and the original dye were detected by an HPLC technique. The HPLC system consisted of a Dionex P580 pump, a UVD 340S diode array detector, and an intersil ODS-3 C$_{18}$ reverse column (5 µm, 250 × 4.6 mm^2). Five intermediates, namely, *N,N*-diethyl-*N'*-ethylrhodamine (DER), *N,N*-diethylrohodamine (DR), *N*-ethyl-*N'*-ethylrhodamine (EER), *N*-ethylrhodamine (ER), and rhodamine (R) were thus identified. LC-MS analyses were carried out using a com-
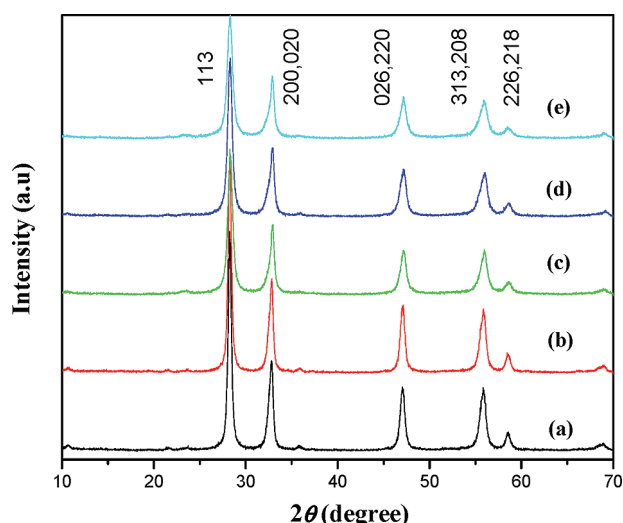

FIGURE 1. XRD patterns of the samples with different R_F values prepared at 180 °C for 24 h. R_F = 0 (a), R_F = 0.1 (b), R_F = 0.2 (c), R_F = 0.4 (d), and R_F = 0.6 (e).

mercial Thermo Finnigan (San Jose CA) LCQ Advantage ion trap mass spectrometer equipped with an ESI ion source. GC-MS analyses were carried out on a Finnigan Trace DSO Ultra instrument equipped with a DB-5 MS capillary column (30 m × 0.25 mm).

3. Results and Discussion

3.1. Catalyst Characterization. X-ray diffraction patterns were used to investigate the changes of the phase structures of the as-prepared samples. Figure 1 shows XRD patterns of the samples prepared by the hydrothermal process. All of the as-prepared samples appeared to be phase-pure Bi$_2$WO$_6$ [JCPDS No. 73-1126]. Further observation showed that the peak intensities of Bi$_2$WO$_6$ became steadily weaker with increasing R_F, and the diffraction peaks of Bi$_2$WO$_6$ were wider, indicating the reducing of crystallization and formation of smaller Bi$_2$WO$_6$ crystallites. The presence of F$^-$ ions could play an important role in the formation of Bi$_2$WO$_6$ crystals. It was well-known that the phase formation of Bi$_2$WO$_6$ crystal occurred due to the rearrangement of WO$_6$ octahedra (*3, 5*). The crystallization process of the Bi$_2$WO$_6$ phase from the amorphous precursors was postulated to initiate through face-sharing polycondensation of these octahedrons. According to the surface acidic/basic properties, the surface Bi−OH group in the Bi$_2$WO$_6$ crystal should be at least partially protonated to give BiOH$_2^+$. Consequently, the free F$^-$ ions liberated in the solution would interact with the small crystal. Nucleophilic substitution was favored due to the high electronegativity of F$^-$ ions, which in turn reduced the chemical reactivity of the precursor. In the process of the crystallization, F$^-$ ions were involved, resulting in the more vacancies in the Bi$_2$WO$_6$ crystal. Although more work is needed to illustrate clearly these rather complex interactions, it is believed that the interaction of these anionic species with the surface Bi^{3+} ion prohibited the enlargement of the crystal nuclei.

Figure 2 shows the nitrogen adsorption and desorption isotherms of the as-prepared samples with varying R_F. The isotherm corresponding to the sample obtained without fluoride was of type IV (BDDT classification) with two capillary condensation steps, implying a bimodal pore size distribution in the mesoporous and macroporous regions. This bimodal mesopore size distribution resulted from two different aggregates in the powders. The hysteresis loop in the lower relative pressure range (0.4 < P/P_0) was related to finer intraaggregated pores formed between
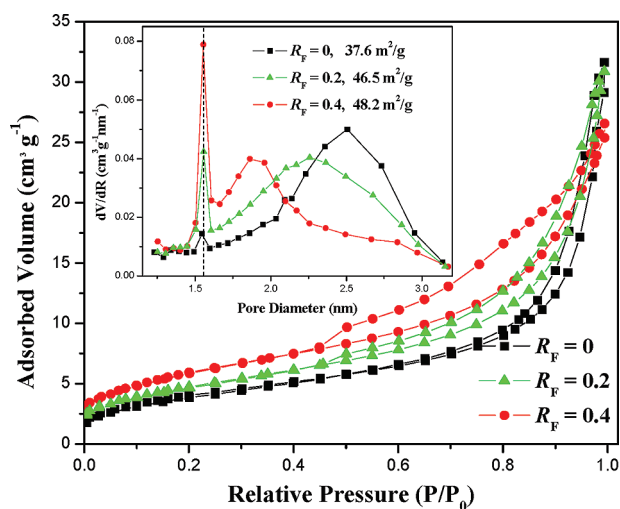
FIGURE 2. Nitrogen adsorption—desorption isotherms of Bi_2WO_6 samples with different R_F values. Inset: Pore size distribution curve of the as-prepared sample.

FIGURE 3. DRS spectra of Bi_2WO_6 samples with different R_F values.

intraagglomerated primary particles, and that in the higher relative pressure range ($0.8 < P/P_0 < 1$) was associated with larger interaggregated pores produced by interaggregated secondary particles (*15*). The bimodal mesopore size distribution was further confirmed by the corresponding pore size distributions shown in the inset of Figure 2. The powder contained small mesopores of ca. 1.6 nm and larger mesopores with a maximum pore diameter of ca. 2.6 nm. The presence of fluoride in the synthetic system exerted a significant influence on the pore structures of the obtained products. With increasing R_F, the isotherms showed higher adsorption at high relative pressures, indicating the formation of the macropores and/or an increasing pore volume. The two separate hysteresis loops gradually joined together as one loop, implying that the pore size distributions of the intraaggregated and interaggregated pores tended to overlap, as confirmed in the inset of Figure 2. Furthermore, the pore volumes of intraaggregated mesopores were negligible compared with those of the interaggregated ones, based on their corresponding integral areas. The BET surface areas of Bi_2WO_6 products were also found to be highly dependent on R_F. Each sample showed a monotonic increase in the BET surface area with increasing R_F, which was in good agreement with the XRD results.

UV—visible DR spectra of the as-prepared samples are shown in Figure 3. The Bi_2WO_6 sample presented the photoabsorption ability from the UV light region to the visible light with a wavelength shorter than 470 nm, which was in good agreement with the previous report (*3*). It was noteworthy that the onsets of the catalysts were dependent strongly on the R_F value. When R_F was ≤0.2, the samples showed the same absorption onset. However, the absorption onsets of the samples were red-shifted apparently, when R_F increased from 0.2 to 0.6. We concluded that the difference of the absorbance edges could arise from the fluorination of Bi_2WO_6 catalyst. For a crystalline semiconductor, it is shown that the optical absorption near the band edge follows the equation $a h\nu = A(h\nu - E_g)^n$, where a, ν, E_g, and A are the absorption coefficient, the light frequency, the band gap, and a constant, respectively (*5*). Among them, n decides the characteristics of the transition in a semiconductor. According to the equation, the value of n for Bi_2WO_6 was 1 from the data in Figure 3. There are two 6s valence electrons of Bi in the crystal. The band gap of the photocatalyst could be estimated from tangent lines in the plots of the square root of the Kubelka—Munk functions against the photon energy, as
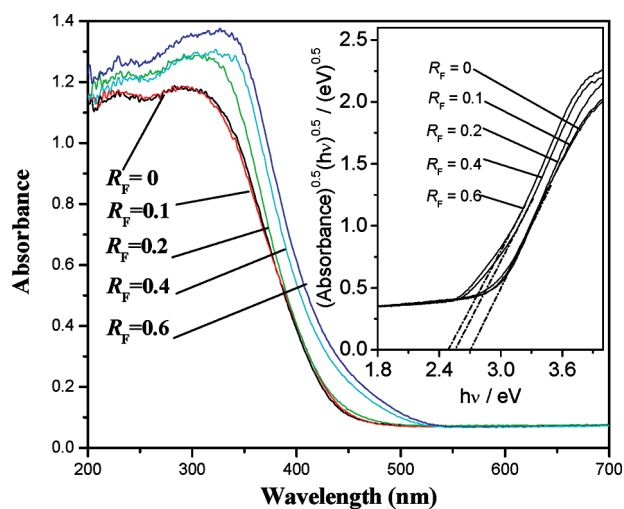
shown in the inset of Figure 3. The band gap of the sample was estimated to be 2.71, 2.71, 2.70, 2.55, and 2.50 eV from the onset of the absorption edge, corresponding to $R_F = 0$, 0.1, 0.2, 0.4, and 0.6, respectively. The color of the sample ($R_F = 0$, 0.1, and 0.2) was pale-yellow, whereas the sample was yellowish in color when $R_F = 0.4$ or 0.6, as predicted from their photoabsorption spectra.

To study the surface properties of the as-prepared samples, the variation of CA under weak UV light irradiation was observed, and the results are shown in Figure S4. Before UV light irradiation, the original CA for the Bi_2WO_6 sample was about 39°. With R_F increasing, CA for the fluorinated Bi_2WO_6 decreased to 12° ($R_F = 0.6$), suggesting that the fluorination greatly improved the duration of hydrophilicity of the material (see Supporting Information, Figure S5). With UV light irradiation, all the samples showed photoinduced hydrophilicity, whereas CA decreased quicker on the sample with smaller R_F in most cases. Hashimoto et al. found that the photoinduced hydrophilicity was due to structural changes of the material surface, completely different from the conventional photocatalytic reaction. The key was the hydroxyl group's reconstruction and that their amount increased on the sample surface under UV light irradiation (*16*). In detail, the photogenerated holes were trapped by surface lattice oxygen atoms, resulting in a breaking of the bonds between oxygen and metal atoms. Subsequently, water molecules dissociatively absorbed at these sites (hydroxyl formation). So the bond strength between oxygen and metal atom was important to the photoinduced hydrophilicity. The fluorination can increase the hydroxyl amount of the surface in the aqueous solution. Meanwhile, because F^- ions have a much stronger affinity for electrons compared with O^{2-} ions, it is postulated that the electronic cloud could deviate from the original position in a Bi—O polyhedron containing fluorine, and the bonds between Bi and O could be weakened in $F-Bi_2WO_6$. Therefore, plenty of oxygen vacancies are easily produced with the illumination of UV light in $F-Bi_2WO_6$. This could undoubtedly improve the photoinduced hydrophilicity. In addition, the fluorinated process could probably increase defects, which is considered to be beneficial to the decrease in the water CA. This could be the reason that the original CA on $F-Bi_2WO_6$ is smaller than that of Bi_2WO_6. The CA experiment revealed that the fluorination remarkably affected the surface properties of Bi_2WO_6 catalyst and could give rise to a great influence on the photochemical properties of Bi_2WO_6 catalyst (*17*).
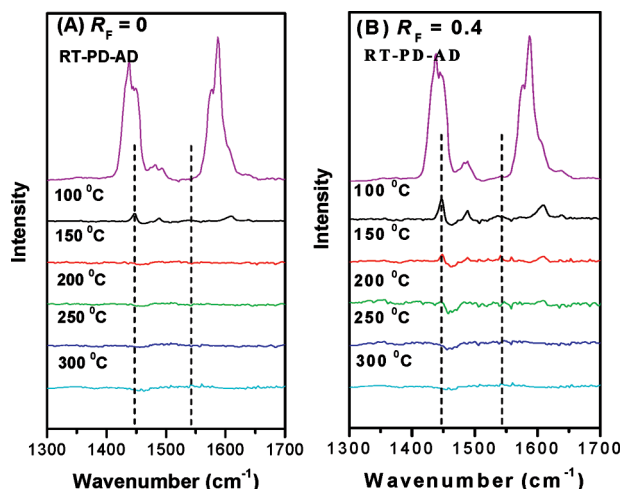
FIGURE 4. FTIR spectra showing the 1300–1700 cm^{-1} region of the thermoprogrammed desorption of pyridine at the different temperatures on the samples of (A) R_F = 0 and (B) R_F = 0.4.

The surface acidity of the as-prepared sample was also examined as a correlation between the surface acidity and photocatalytic activity of the photocatalysts. The adsorption of pyridine, monitored by FTIR, was chosen as a probe reaction to characterize the surface acidity. The results are shown in Figure 4. The peaks at the range of 1400–1650 cm^{-1} were ascribed to the pyridine ring-stretching modes. Upon the interaction with a Brönsted acid, pyridine was protonated and absorbed at a specific IR wavelength around 1540–1545 cm^{-1}, as well as at several other specific wavelengths not discussed here. Following interaction with a Lewis acid site, pyridine would also form a coordinatively bonded complex with a specific IR absorption band centered at 1445 cm^{-1} (18). Therefore, the bands at 1541 and 1440 cm^{-1} observed for both samples could be assigned to the coordinated pyridine adsorbed on the Brönsted acid and Lewis acid surface sites, respectively. With the increase of temperature to 150 °C, the peaks at 1541 and 1440 cm^{-1} on the Bi$_2$WO$_6$ sample disappeared swiftly. However, in the F−Bi$_2$WO$_6$ case, these bands disappeared completely only when the sample was treated at 200 °C. This result indicated that the fluorinated Bi$_2$WO$_6$ has stronger acid sites, and enhanced acidity of the surface, which could contribute to higher photoactivity.

3.2. Photodegradation of RhB and Identification of the Intermediates. The RhB photodegradation over the as-prepared samples under the simulative sunlight (>290 nm) is shown in Figure S6. The photodegradation of RhB under the simulative sunlight without a catalyst was insignificant. The photoactivity of the sample was strongly dependent on the R_F value. With R_F increasing from 0 to 0.4, the photoactivity of the sample for the RhB photodegradation was enhanced. With the exclusion of the sample (R_F = 0.6), the as-prepared sample showed higher photoactivities for the RhB degradation than that of P25 (TiO$_2$). The maximum photoactivity was observed for the sample (R_F = 0.4). When R_F further increased to 0.6, the photoactivity of the sample instead decreased. Although it presented a surface area (51.3 m^2/g) similar to that of the sample of R_F = 0.4 (48.2 m^2/g), their photocatalytic activity was fairly different. Therefore, it was inferred that the specific surface areas played a minor role in this photochemical process.

The temporal evolution of the spectral changes taking place during the photodegradation of RhB over Bi$_2$WO$_6$ (R_F = 0) and F−Bi$_2$WO$_6$ (R_F = 0.4) is shown in Figure 5, parts A and B, respectively. Tetraethylated rhodamine shows a major absorption band at 553 nm. In both cases, the simulative sunlight irradiation (λ > 290 nm) on the aqueous RhB/catalyst suspensions resulted in an apparent decrease in the absorp-

tion. It was well-reported that the RhB photodegradation occurred via two competitive processes: *N*-demethylation and the destruction of the conjugated structure (19, 20). In the case of Bi$_2$WO$_6$ catalyst, the absorption maximum of the suspension decreased by 92% in the presence of Bi$_2$WO$_6$ catalyst after irradiation for 300 min, and the band shifted from 553 to 515 nm. The color of the suspension changed directly from pink to light red. By contrast, the absorption maximum of the degraded solution exhibited concomitant, slight hypsochromic shifts in the presence of F−Bi$_2$WO$_6$. However, the hypsochromic shifts of the absorption maximum were more pronounced than those observed with the Bi$_2$WO$_6$ system. This hypsochromic shift of the absorption band was presumed to result from the formation of a series of *N*-deethylated intermediates in a stepwise manner (19). After the irradiation for 210 min, ca. 98% of RhB was degraded in the F−Bi$_2$WO$_6$ system and the spectral maximum shifted somewhat from 553 to 500 nm. The color of the suspension changed gradually from pink to light green. Further irradiation caused the decrease of the absorption band at 500 nm, and the color of the suspension changed sequentially colorless. This indicated that the fluorination of Bi$_2$WO$_6$ changed not only the photodegradation rate of the pollutant but also the mechanistic pathways of the pollutant degradation. The fluorinated Bi$_2$WO$_6$ enhanced significantly the ratio of the deethylation process to the cleavage of the chromophore structure.

Intermediates of RhB during the photodegradation were monitored by the HPLC technique, and the results are illustrated in Figure 5C,D, respectively. The RhB dye used here was of 97% purity with a DER percentage of ca. 3%, which was consistent with the HPLC analysis. During the photoreaction in the Bi$_2$WO$_6$ system, only the first mono *N*-deethylated intermediate was clearly observed, following which DER degraded rapidly. A small amount of the second *N*-deethylated intermediate was also detected; however, no other deethylated intermediates was observed clearly (see Supporting Information, Figure S7). Furthermore, some new peaks emerged after the reaction continued for 210 min. These peaks were supposed to represent some highly polar components that could not by separated by the HPLC technique, and these components were most likely small-molecule intermediates. In the case of F−Bi$_2$WO$_6$ catalyst, four intermediates were observed, namely, DER, EER, DR, and ER corresponding to the peaks of b, c, d, and e, respectively, which resulted from losing one and/or two ethyl groups from the xanthene ring in the parent RhB structure, as we have definitely determined with LC-MS (see Supporting Information, Figure S8), which was also in agreement with the previous report (20). An insignificant amount of the complete *N*-deethylated product could also be observed after 180 min irradiation. In Figure 5C, with the quick disappearance of RhB, the concentrations of DER, EER, and DR species increased slightly and then decreased with further irradiation. The first product of *N*-deethylation reached its maximum concentration after a 45 min irradiation period, whereas the maximum of the final *N*-deethylated product appeared after the irradiation for 180 min, which proved more RhB molecules were degraded by the *N*-demethylation process in the F−Bi$_2$WO$_6$ system as compared to the Bi$_2$WO$_6$ system.

To obtain more information about the highly polar and small molecular weight intermediates that could not be separated and identified by HPLC, the products were further analyzed by a GC-MS technique. The major final products in the presence of Bi$_2$WO$_6$ or F−Bi$_2$WO$_6$ detected are listed in Figure S9 (see Supporting Information). They were mainly formic acid, phthalic acid, and phthalic anhydride. Many *N*-containing compounds with small molecular weight were also observed, which indicated that the *N*-containing fraction of the RhB molecule could first be attacked by the active
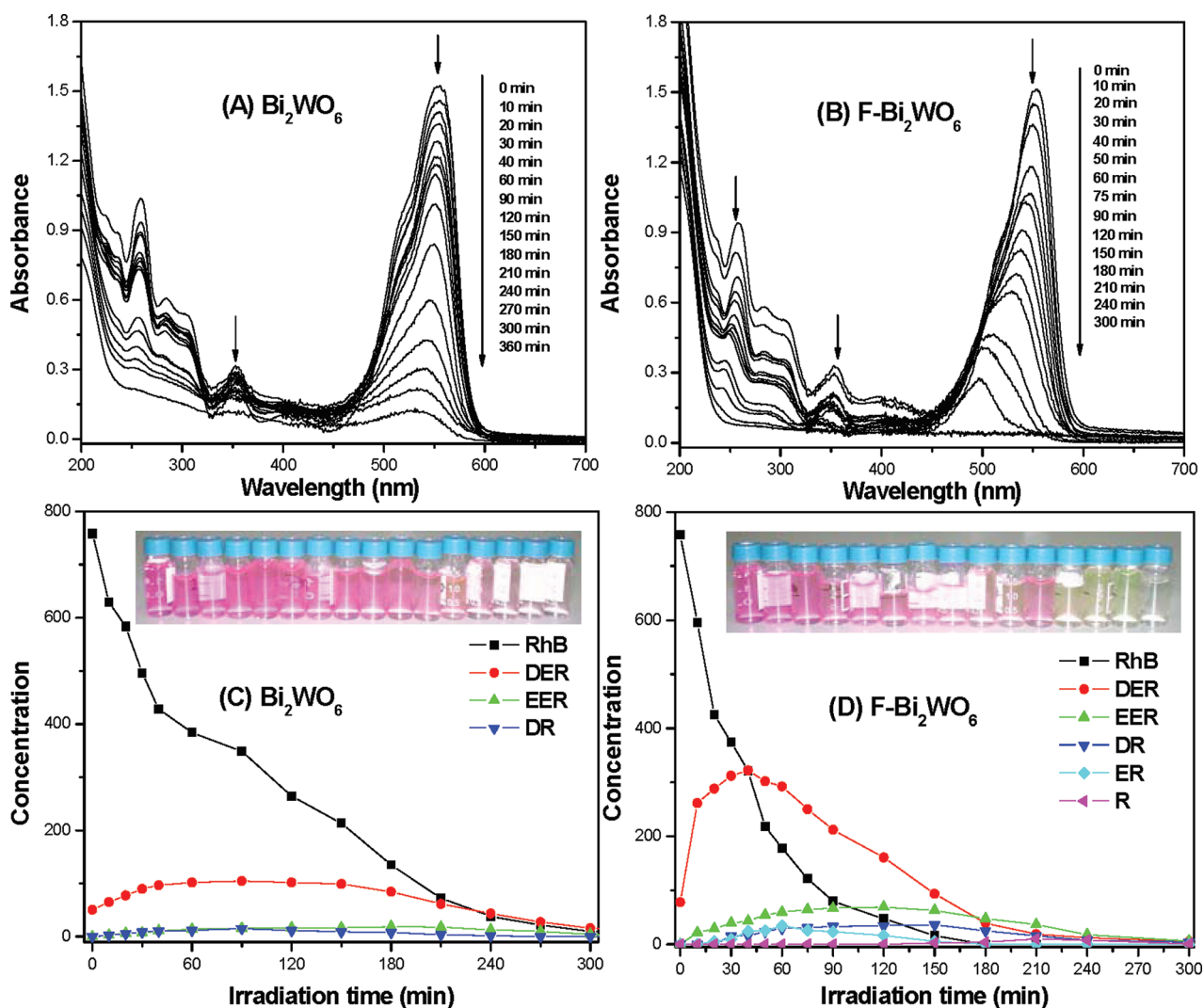
FIGURE 5. UV—visible spectral changes of RhB (2×10^{-5} M, 50 mL) over the catalysts, (A) $R_F = 0$ and (B) $R_F = 0.4$. Variations in the distribution of the intermediate products in the corresponding suspensions, (C) $R_F = 0$ and (D) $R_F = 0.4$. The concentrations of the *N*-dealkylated intermediates were determined by the corresponding peak areas gained from the HPLC technique.

species, and the RhB molecules were degraded subsequently. The GC-MS analysis provided solid evidence for the cleavage of the conjugated xanthene structure of both RhB and the deethylated intermediates during the degradation reaction in the presence of two photocatalytic systems.

3.3. The Proposed Mechanism. On the basis of the DRS results, it could be speculated that F^- ions incorporated into the structure of Bi_2WO_6 prepared by a fluoride-mediated hydrothermal process. These F^- ions may be positioned in the crystal lattice, may be an interstitial impurity, ad/or may be adsorbed on the surface.

X-ray diffraction patterns illustrated that the doping with fluorine did not result in the development of new crystal orientations or a change in preferential orientations. Hence, independent of the presence or absence of fluorine, the samples were the pure aurivillius Bi_2WO_6 phase. However, a careful comparison of the (113) diffraction peaks in the range of $2\theta = 27.5$–$29.5°$, as shown in Figure S10, the peak position of Bi_2WO_6 with different fluorine contents shifted slightly toward a higher 2θ value. The same results were also presented in the other diffraction peaks. According to Bragg's law, $d_{(hkl)} = \lambda/(2 \sin \theta)$, where $d(hkl)$ is the distance between crystal planes of (hkl), λ is the X-ray wavelength, and θ is the diffraction angle of the crystal plane (hkl) *(18)*. The ionic radius of F^- (0.133 nm) is smaller than that of O^{2-} (0.140 nm); the decrease in lattice parameters ($d(hkl)$ value) should result

in the increase in 2θ values. Therefore, the observed shift of the diffraction peaks toward higher angles could be due to the smaller lattice parameter expected for the substitution of O^{2-} by F^-. Instead, F^- doping as the interstitial dopants could lead to an increase in lattice parameter due to repulsion between F^- anions, which has been observed from the fluorinated $ZnWO_4$ in our previous report *(8)*. Accompanied by F^- doping, surface fluorination of Bi_2WO_6 occurred concurrently, which could be concluded from Figures 3 and 4. Therefore, the enhanced photoactivity of F–Bi_2WO_6 could be a synergetic effect of surface modification and bulk doping by F^- ion.

The Bi_2WO_6 formation was a typical hydrothermal ripening process: a highly supersaturated solution was adopted, and the amorphous fine particles acted as the precursor for the synthesis of crystallized Bi_2WO_6. In the beginning, the formation of tiny crystalline nuclei in a supersaturated medium occurred, and the crystal growth then followed. The larger particles grew at the cost of the small particles, according to the well-known Gibbs—Thomson law. This speculation has been proved by the TEM observation in our previous report *(5)*. In the present condition, F^- ions were introduced from the precursor of fluorinated Na_2WO_4, which was synthesized from WO_3, Na_2O, and NaF by the high-temperature solid-state reaction. One fraction of F^- ions by the substitution of O^{2-} in the crystal lattice of Na_2WO_4 could

be directly introduced to the resulting sample as the doping of the crystal lattice. Instead, the other fraction of F^- ions could be liberated into the solution in the hydrothermal process. It is well-known that the aurivillius structure of Bi_2WO_6 consists of alternating fluorite-like $[Bi_2O_2]^{2+}$ layers and $[WO_4]^{2-}$ layers which comprise the corner-linked octahedral units. Due to the high electron density of F^- ions, there is a strong repulsion between F^- and $[WO_4]^{2-}$. Thus, the dissolution of F^- ions into the interstitial lattice between $[Bi_2O_2]^{2+}$ layers and $[WO_4]^{2-}$ layers is limited. However, this fraction of F^- ions could interact strongly with the surface of the Bi_2WO_6 crystal, which prohibited the enlargement of the crystal, and enhanced the surface acidity of the Bi_2WO_6 catalyst.

A few researchers have reported the improvement of photocatalytic activity by the fluorination of TiO_2 powders (*9–13, 21*). This high photocatalytic activity was ascribed to several beneficial effects produced by the F^- ion doping in bulk TiO_2 crystal: enhancement of the crystallinity, creation of oxygen vacancies, or increase of active sites by conversion of some Ti^{4+} to Ti^{3+}. As for the surfaced fluorination of TiO_2, the enhanced photoactivity of TiO_2 was commonly ascribed to higher surface acidity, enhanced generation of mobile free OH radicals, and surface oxygen vacancies. In this case, the resulting Bi_2WO_6 sample prepared by a fluoride-mediated synthesis showed the pure aurivillius phase but a fall in the crystallinity. Since the production of $^\bullet$OH in the present system was almost impossible from the theoretical viewpoint due to the standard redox potential of Bi^V/Bi^{III} being more negative than that of $^\bullet$OH/OH$^-$(+1.99) (*3*). The enhanced photoactivity of the as-prepared sample could not be ascribed to the generation of mobile free OH radicals. On the CA experiment, the as-prepared samples showed the enhancement of the surface acidity, which could be one of the reasons that fluorinated Bi_2WO_6 showed higher photoactivity for the RhB degradation. The catalyst with an acidic surface could easily adsorb polarized organic reactants and thus promote their photocatalytic decomposition. The enhanced hydrophilicity of the as-prepared sample could also be attributed to more oxygen vacancies, which was considered to be beneficial to the photoactivity of the catalyst. Beyond that, the absorption spectra of the as-prepared sample showed a stronger absorption in the UV−visible range and a red shift in the band gap transition. Therefore, the fluorination of Bi_2WO_6 increased the number of photogenerated electrons and holes to participate in the photocatalytic reaction, which could partly explain the enhanced photoactivity. Following this general information, we assume that the enhanced photoactivity of F−Bi_2WO_6 could be a synergetic effect, including more oxygen defects, enhancement of surface acidy, and light absorbance.

In the present study, the fluorination of Bi_2WO_6 affected not only the rate but also the mechanistic pathways of the RhB degradation. In the Bi_2WO_6-mediated photocatalysis, the degradation of RhB was completely ascribed to a photochemical process involved by photoinduced holes. Furthermore, there could be two photochemical mechanisms, namely, a photocatalytic process and a photosensitized process. On one hand, Bi_2WO_6 was an active photocatalyst, and RhB could be degraded by the direct interaction with a strong oxidizing hole originating from the hybridization of the Bi6s and O2p orbitals. The RhB molecule was attacked and then degraded via the destruction of the conjugated structure. On the other hand, RhB dye could absorb the visible light, which was attributed to the ground state and the excited state of the dye. Therefore, RhB could be degraded by a photosensitized process. In this process, the degradation of RhB did not involve any VB hole; mineralization of dyes found its origins with the active oxygen radical species, $O_2^{\bullet-}$, and the radical cations, dye$^{\bullet+}$. The photosensitized degradation

of RhB was commonly via the *N*-demethylation process (*19*). Compared to the photocatalytic process, the photosensitized process required the stronger interaction between the dye and the Bi_2WO_6 catalyst, which was beneficial to the transfer of photoinduced electron. The F-containing function on the fluorinated surface seemed to serve as an electron-trapping site and enhanced interfacial electron-transfer rates by tightly holding trapped electrons. As a result, more RhB molecules were degraded via the *N*-demethylation process. It has been reported that the surface fluorination of TiO_2 by the displacement of OH by F^- ions changed the surface interactions. Then, the rate of electron scavenging by O_2 and superoxide formation would be influenced (*21*).

Supporting Information Available
XRD patterns of F−Na_2WO_4, TEM, HRTEM, and CA variation of F−Bi_2WO_6, photodegradtion of RhB, HPLC, LC-MS, and GC-MS analysis of the intermediate products, and diffraction peak variation of F−Bi_2WO_6, Figures S1–S10. This material is available free of charge via the Internet at http://pubs.acs.org.

Literature Cited

(1) Hoffmann, M. R.; Martin, S. T.; Choi, W.; Bahnemann, D. W. Environmental applications of semiconductor photocatalysis. *Chem. Rev.* **1995**, *95*, 69–96.

(2) Zhu, S.; Xu, T.; Fu, H.; Zhao, J.; Zhu, Y. Synergetic effect of Bi_2WO_6 photocatalyst with C_{60} and enhanced photoactivity under visible irradiation. *Environ. Sci. Technol.* **2007**, *41*, 6234–6239.

(3) Fu, H.; Pan, C.; Yao, W.; Zhu, Y. Visible-light-induced degradation of rhodamine B by nanosized Bi_2WO_6. *J. Phys. Chem. B* **2005**, *109*, 22432–22439.

(4) Fu, H.; Yao, W.; Zhang, L.; Zhu, Y. Photocatalytic properties of nanosized Bi_2WO_6 catalysts synthesized via a hydrothermal process. *Appl. Catal., B* **2006**, *66*, 100–110.

(5) Zhang, C.; Zhu, Y. Synthesis of square Bi_2WO_6 nanoplates as high-activity visible-light-driven photocatalysts. *Chem. Mater.* **2005**, *17*, 3537–3545.

(6) Yu, J. G.; Xiong, J. F.; Cheng, B.; Yu, Y.; Wang, J. B. Hydrothermal preparation and visible-light photocatalytic activity of Bi_2WO_6 powders. *J. Solid State Chem.* **2005**, *178*, 1968–1972.

(7) Fu, H.; Lin, J.; Zhang, L.; Zhu, Y. Synthesis and photocatalytic activities of $ZnWO_4$ nanorod. *Appl. Catal., A* **2006**, *306*, 58–67.

(8) Huang, G.; Zhu, Y. Enhanced photocatalytic activity of $ZnWO_4$ catalyst via fluorine doping. *J. Phys. Chem. C* **2007**, *111*, 11952–11958.

(9) Hattori, A.; Shimoda, K.; Tada, H.; Ito, S. Photoreactivity of sol−gel TiO_2 films formed on soda-lime glass substrates: effect of SiO_2 underlayer containing fluorine. *Langmuir* **1999**, *15*, 5422–5425.

(10) Yu, J. C.; Yu, J. G.; Ho, W.; Jiang, Z.; Zhang, L. Effects of F^- doping on the photocatalytic activity and microstructures of nanocrystalline TiO_2 powders. *Chem. Mater.* **2002**, *14*, 3808–3816.

(11) Li, D.; Haneda, H.; Hishita, S.; Ohashi, N.; Labhsetwar, K. N. *J. Fluorine Chem.* **2005**, *126*, 69–77.

(12) Vohra, S. M.; Kim, S.; Choi, W. Effects of surface fluorination of TiO_2 on the photocatalytic degradation of tetramethylammonium. *J. Photochem. Photobiol., A: Chem.* **2003**, *160*, 55–60.

(13) Park, H.; Choi, W. Effects of TiO_2 surface fluorination on photocatalytic reactions and photoelectrochemical behaviors. *J. Phys. Chem. B* **2004**, *108*, 4086–4093.

(14) Wang, J. S.; Yin, S.; Zhang, Q. W.; Saito, F.; Sato, T. Mechanochemical synthesis of $SrTiO_3$-xFx with high visible light photocatalytic activities for nitrogen monoxide destruction. *J. Mater. Chem.* **2003**, *13*, 2348–2352.

(15) Yu, J. G.; Liu, S.; Yu, H. Microstructures and photoactivity of mesoporous anatase hollow microspheres fabricated by fluoride-mediated self-transformation. *J. Catal.* **2007**, *249*, 59–66.

(16) Mryauchi, M.; Nakajima, A.; Watanabe, T.; Hashimoto, K. Photocatalysis and photoinduced hydrophilicity of various metal oxide thin films. *Chem. Mater.* **2002**, *14*, 2812–2816.

(17) Tang, J.; Quan, H.; Ye, J. Photocatalytic properties and photo-induced hydrophilicity of surface-fluorinated TiO_2. *Chem. Mater.* **2007**, *19*, 116–122.

(18) Platon, A.; Thomson, W. J. Quantitative Lewis/Brönsted ratios using DRIFTS. *Ind. Eng. Chem. Res.* **2003**, *42*, 5988–5992.

(19) Lei, P.; Chen, C.; Yang, J.; Ma, W.; Zhao, J.; Zang, L. Degradation of dye pollutants by immobilized polyoxometalate with H_2O_2 under visible-light irradiation. *Environ. Sci. Technol.* **2005**, *39*, 8466–8474.

(20) Chen, C.; Zhao, W.; Li, J.; Zhao, J. Formation and identification of intermediates in the visible-light-assisted photodegradation of sulforhodamine-B dye in aqueous TiO_2 dispersion. *Environ. Sci. Technol.* **2002**, *36*, 3604–3611.

(21) Calza, P.; Pelizzetti, E.; Mogyorosi, K.; Kun, R.; Dekany, I. Size dependent photocatalytic activity of hydrothermally crystallized titania nanoparticles on poorly adsorbing phenol in absence and presence of fluoride ion. *Appl. Catal., B* **2007**, *72*, 314–321.